Journal Name

ARTICLE TYPE

Cite this: DOI: 10.1039/xxxxxxxxxx

Experimental and theoretical XPS and NEXAFS studies of *N*-methylacetamide and *N*-methyltrifluoroacetamide

Cui Li,[a,b] Peter Salén,[c] Vasyl Yatsyna,[d] Luca Schio,[e] Raimund Feifel,[d] Richard Squibb,[d] Magdalena Kamińska,[c] Mats Larsson,[c] Robert Richter,[f] Michele Alagia,[e] Stefano Stranges,[g,e] Susanna Monti,[a,h] Vincenzo Carravetta,[b†] and Vital Zhaunerchyk[d‡]

Received Date
Accepted Date

DOI: 10.1039/xxxxxxxxxx

www.rsc.org/journalname

Experimental Near-Edge X-ray Absorption Fine-Structure (NEXAFS) spectra of *N*-methyltrifluoroacetamide (FNMA), which is a peptide model system, measured at the C, N, O and F K-edges are reported. The features in the spectra have been assigned by Static-Exchange (STEX) calculations. Using the same method, we have also assigned previously measured NEXAFS spectra of another peptide model system, *N*-methylacetamide (NMA). To facilitate the NEXAFS feature assignments, X-ray Photoelectron Spectroscopy (XPS) measurements for NMA and FNMA have been carried out with the aim to obtain the 1s electron ionization potentials, which are compared with the values predicted by our Hartree-Fock (ΔHF) and Multi Configuration Self Consistent Field (ΔMCSCF) calculations. We also demonstrate an approach to compensate for screening effects that are neglected in the STEX method. Ion yield measurements of FNMA associated with excitation of several C, N, O, and F K-shell pre-edge resonances have revealed site-specific fragmentation in some cases which we interpret with the aid of our theoretical calculations.

1 Introduction

Synchrotron radiation based Near-Edge X-ray Absorption Fine-Structure (NEXAFS) spectroscopy is a highly sensitive technique to probe electronic structure of molecules in gas-phase or on surfaces.[1] The advantage of gas-phase studies is that they enable investigation of intrinsic properties of molecules by avoiding contributions from inter-molecular or surface atoms interactions. In NEXAFS, an electron from a core orbital is excited to an unoccupied molecular orbital (UMO) which is followed by Auger decay or X-ray photon emission. For molecules consisting of light elements, such as C, N, and O, the former is the most common decay pathway. Upon resonant core-valence excitation and subsequent Auger decay, the final state of the molecule is often repulsive, which leads to fragmentation. This implies that the NEXAFS technique, in addition to being useful for probing the electronic structure, can also be used in mass spectrometry. In contrast to many existing mass spectrometry methods, in which the excitation energy is randomized over all degrees-of-freedom such that fragmentation proceeds in a statistical manner,[2–7] molecular fragmentation patterns upon resonant core-excitation and subsequent Auger decay may depend on the initial excitation energy. Such a behavior can be explained by a spectator-type Auger decay, in which the core electron excited to an anti-bonding UMO is not involved in the Auger decay, implying that the "memory" of the initial excitation step might be preserved.[8–14] We note that fragmentation of core ionized molecules is expected to be less site-specific because an anti-bonding orbital is not populated directly, though some site-specificity was also reported[15–19].

Modern synchrotron radiation sources enable highly accurate NEXAFS measurements with an ultimate resolution determined by the core-hole lifetime reflected in the corresponding natural linewidth of *e.g.*, ≈160 meV and ≈115 meV for O 1s and N 1s hole states, respectively[20–24]. On the theoretical side, nowadays

[a] *Theoretical Chemistry and Biology, School of Biotechnology, Royal Institute of Technology, 10044 Stockholm, Sweden.*
[b] *CNR-IPCF, Institute of Chemical Physical Processes, via G. Moruzzi 1, I-56124 Pisa, Italy.*
[c] *Department of Physics, Stockholm University, 106 91 Stockholm, Sweden.*
[d] *Department of Physics, University of Gothenburg, 412 96 Gothenburg, Sweden.*
[e] *IOM-CNR Tasc, SS-14, Km 163.5 Area Science Park, Basovizza, I-34149 Trieste, Italy.*
[f] *Elettra - Sincrotrone Trieste, Area Science Park, 34149 Basovizza, Trieste, Italy.*
[g] *Dipartimento di Chimica e Tecnologie del Farmaco, Universitá Sapienza, Roma, I-00185 Italy.*
[h] *CNR-ICCOM, Institute of Chemistry of Organometallic Compounds, via G. Moruzzi 1, I-56124 Pisa, Italy.*
† carravetta@ipcf.cnr.it
‡ vitali.zhaunerchyk@physics.gu.se

NEXAFS spectra can be modeled[25–33] with an accuracy up to a few tenths of an eV for small molecules. For large systems the calculations can also provide quite accurate estimates enabling assignment of the main features of a NEXAFS spectrum. Due to their quasi stationary character, the energy of core ionized/excited states can in principle be obtained by a number of quantum chemical methods developed for the low energy excited electronic states and modified to avoid variational collapse; most commonly the simple independent particle approximation has been applied for the calculation of transition intensities. The independent particle methods provide an appealing, although approximate, picture of the excitation process because they assign an individual excited orbital to each line in the electronic spectrum. One such method, which enables proper assignment of NEXAFS features, is the Static Exchange (STEX) technique that has been instrumental in interpreting a large number of NEXAFS spectra of molecules in different phases[30].

In this work we report experimental *K*-shell NEXAFS spectra of *N*-methyltrifluoroacetamide (FNMA), $CH_3NHCOCF_3$, measured at the C, N, O and F *K*-edges, together with mass spectra of FNMA associated with the excitation of different NEXAFS resonances. In one of our previous works[8] we have reported *K*-shell C-, N-, and O-edge NEXAFS spectra of *N*-methylacetamide (NMA), $CH_3NHCOCH_3$, which has a molecular structure similar to FNMA (Fig. 1) with the difference that in FNMA the methyl group located next to the CO-group is substituted with CF_3. NMA and FNMA are biologically relevant molecules as they contain a peptide link, -CO-NH-, through which amino acids are coupled together to form peptides and proteins. To assign features in the NEXAFS spectra of NMA and FNMA we have performed numerical calculations with the STEX technique, results of which are presented here as well. We have also carried out XPS (X-ray Photoelectron Spectroscopy) measurements to obtain the 1*s* electron binding energies for NMA and FNMA to be compared to the values predicted by our Hartree-Fock (ΔHF) and Multi Configuration Self Consistent Field (ΔMCSCF) calculations. The ionization thresholds are crucial quantities for an effective comparison of theoretical calculations and experimental photoabsorption measurements.

2 Experimental description

The measurements have been performed at the GasPhase beamline[34] of the Elettra synchrotron radiation facility, Italy. NMA and FNMA have been obtained commercially with a specified purity better than 99 %. The vapor pressure of both molecules at room temperature is sufficiently high to deliver sample to the interaction region using an effusive source without additional heating. The X-ray photon energy was tuned by varying the gap of the beamline undulator and scanning the monochromator. Typically the energy bandwidth was set to ≈200 meV. A commercial hemispherical electron energy analyzer (VG 220i) and a home-built ion time-of-flight mass spectrometer were used to measure the XPS spectra and ion mass spectra, respectively. The XPS spectra were recorded for both NMA and FNMA at photon energies of 382 eV, 495 eV, and 628 eV, and for FNMA an additional measurement was performed at 770 eV. The NEXAFS spectra were

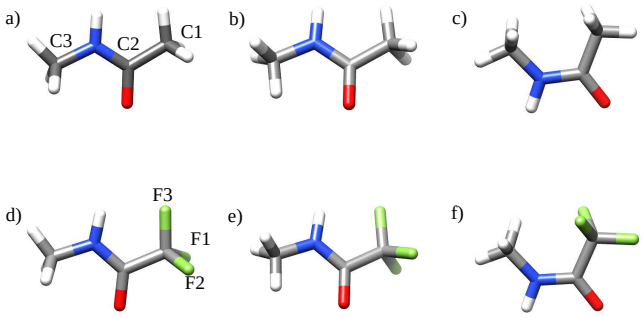

Fig. 1 DFT B3LYP optimized geometries of the three lowest energy structures for NMA (a-c) and FNMA (d-e). The structures presented in (a,b,d,e) and (c,f) are of *trans*- and *cis*-configurations, respectively.

obtained by monitoring the total ion and electron yields in the vicinity of the C, N, O and F *K*-shell edges. They are normalized to the photon flux which was monitored by a photodiode. The XPS and NEXAFS spectra were calibrated by admitting various calibration gases to the experimental chamber, for which the 1*s* electron binding energies and NEXAFS spectra are known.[35–40] In particular, the NEXAFS spectra were calibrated to the absorption spectra of CO_2 for the C 1*s* and O 1s edges,[39] to that of N_2 for the N 1*s* edge,[40] and to that of Xe for the F 1*s* edge[38]. To calibrate the C 1*s*, N 1*s* and F 1*s* XPS spectra we used CO_2[35], N_2[36], and Xe[38] gases, respectively. CO_2[37] was also used to calibrate the O 1*s* XPS spectra. For FNMA, the ion mass spectra were measured at fixed photon energies corresponding to specific *K*-shell excitations. To account for possible non-resonant contributions, originating for example from valence and/or core ionization processes, the mass spectra were also acquired at photon energies just below the pre-edge resonances. All mass spectra have been binned by $m/z = 0.1$. The mass spectrum at 401.6 eV excitation energy showed some signs of residual N_2 indicated by stronger peaks at $m/z = 14$ and 28. Hence, these peaks where excluded in integrated intensities of the spectra used for the normalization with respect to different excitation energies, for all excitation energies.

3 Computational details

For both molecules, ionization potentials (IPs) and absorption spectra at the C, N, O and F *K*-edge have been calculated with the ΔHF and STEX[28] methods, respectively, by using the DALTON code in the independent particle approximation[41], and the basis set Ahlrichs-VTZ[47]. The ΔHF approach, fully including the electronic relaxation and the localization of almost equivalent atoms, like the C atoms of the methyl groups in NMA and the F atoms in FNMA, leads to valuable predictions of the binding energy. The electron correlation effect neglected by the ΔHF approach, giving a minor contribution with respect to the electron relaxation effect, can be remedied by multi-configurational methods like ΔMCSCF.[30] The numbers for describing our MCSCF RAS calculations of ground and core hole state are: for NMA: 10 ac-

tive and 10 excited orbitals for 20 active electrons, corresponding to a total number of 14251 singlet configurations for describing the ground state, 11 active orbitals and 10 excited orbitals for 21 active electrons, generating 23351 doublet configurations for the core hole state; for FNMA: 16 active and 10 excited orbitals are used for 32 active electrons, and then 36721 singlet configurations are generated for the ground state, 15 active orbitals and 10 excited orbitals for 31 active electrons, which correspond to 53026 doublet configurations, are employed in the core hole state calculation. The STEX approach is based on the static exchange approximation, which[42] is an independent particle, independent channel model where the core excitation energy is obtained by adding the ionic target energy to an eigenvalue of a specific one electron hamiltonian describing the motion of the excited/ionized electron in the field of the ion. Compared with previous applications of the static-exchange approximation,[43,44] STEX fully exploits the main advantages of such an approximation, namely an optimized description of the excited/ionized electron motion in an *ab initio* non local potential by projection and full diagonalization of the one-electron hamiltonian on almost complete L^2 basis sets. This is performed by a modern direct approach,[28,30] in a code that is then easily applicable to systems with a large number of electrons. Although the STEX approach fully accounts for the electronic relaxation, this is assumed to be independent from the excited electron, *i.e.*, the screening effect of the excited electron on the target ion is neglected. The energy scale for the bound excitations may then be compressed against the ionization threshold. It is generally assumed that such an error is roughly constant for the different excitation channels and, for easier comparison with the experiment, an energy shift is applied to the theoretical spectrum in order to match, usually, the most intense band. This pragmatic procedure, however, is not always justified and the present spectra at the C *K*-edge provide, as will be discussed in the following, an example of its partial failure. In the case of absorption spectra, due to core excitations from several chemically shifted sites (excitation channels), the approximation of comparable errors for missing or unpaired inclusion of electron correlation and relativistic effects is well justified. However, other errors, like the missing screening effect due to the excited electron in the STEX and similar methods, in addition to being excitation state specific, can also be site specific. A simple way of estimating such errors is to compare the LUMO excitation energy for a specific excitation channel (site) as obtained by STEX with a small (minimal number of determinants) MCSCF calculation that leads to a fully relaxed final state. The result of such calculations are presented in Tab. 1.

Table 1 Theoretical and experimental IPs (eV) of NMA and FNMA, and screening-effect energy correction of the $1s \rightarrow$LUMO transition for NMA and FNMA.

Molecule	*K*-edge	IP (eV)			Corr. (eV)
		Exp.	ΔHF	ΔMCSCF	
NMA	O	536.98	536.27	536.43	-1.71
	N	405.75	406.02	405.92	-0.90
	C1	290.99	291.77	290.21	-0.71
	C2(=O)	293.72	295.19	293.92	-2.63
	C3	291.74	292.37	291.98	-0.70
FNMA	O	537.97	537.86	537.79	-1.63
	N	406.66	407.29	407.05	-1.47
	C1(-F)	298.52	300.48	299.48	-1.92
	C2(=O)	294.55	296.99	295.61	-2.47
	C3	292.37	293.28	292.81	-0.73
	F1	694.59	693.88	694.03	-2.01
	F2	694.59	693.88	694.02	-2.01
	F3	694.59	693.94	694.10	-2.69

4 Results and discussions

4.1 NMA and FNMA conformers

The NMA and FNMA molecules exhibit rotational isomerism and can assume different conformations. A previous study[45] with relatively low accuracy HF calculations has identified a small number of stable conformers with comparable total energy. All these conformers are of *trans*-type, *i.e.*, the oxygen atom of the carbonyl group and hydrogen atom of the NH group are located on opposite sides with respect to the C-N bond. Conformers with a *cis*-geometry have higher energy and are generally considered to be present in a minute amount in the gas phase at room temperature. In order to obtain deeper insight into the stability of different NMA and FNMA conformers under the conditions of the present experimental studies, we have optimized the geometry of both molecules with a higher precision method, namely, calculations based on density functional theory (DFT) with the B3LYP functional[46] and the TZV basis set[47] using the program GAMESS[48]. The results of our calculations for both molecules shown in Fig. 1 suggest the existence of only two stable *trans*-type conformers with very similar total energies. They have different relative orientations of methylic hydrogen atoms and the energy difference between them is on the order of hundredths of kcal/mol. This implies that these conformers will have similar populations at room temperature. The *cis*-type conformer is predicted to be about 2.3 kcal/mol for NMA and 4.1 kcal/mol for FNMA above the *trans*-structures, indicating that at room temperature less than 2% of the molecules in the gas sample have *cis*-geometries. In a very recent study[25] the NEXAFS spectra of NMA at the C, N and O *K*-edge have been compared to theoretical calculations by the TDDFT method[26,29] adopting a *cis*-configuration of the molecule. The authors employed a geometry optimization procedure very similar to the one used by us but, unfortunately, do not discuss the relative stability of the *cis*- and *trans*-type conformers of NMA.

Since UMOs are typically delocalized and the total energy difference between different conformers is vanishingly small compared with the X-ray photon energies, NEXAFS spectra are expected to be generally non-conformer-specific, though some exceptional cases have been reported[49]. In order to verify whether NEXAFS spectra of the lowest two *trans*-type conformers are indistinguishable, we have calculated the NEXAFS spectra for NMA and FNMA in these molecular configurations by the ΔHF and STEX methods. As an example, the NEXAFS spectra calculated for the two lowest energy structures of *trans*-NMA at the O *K*-edge are presented in Fig. 2(a). The differences in the NEXAFS spectra are extremely small which implies that any conformational effect will barely be visible in the experimental data. Therefore, the IP

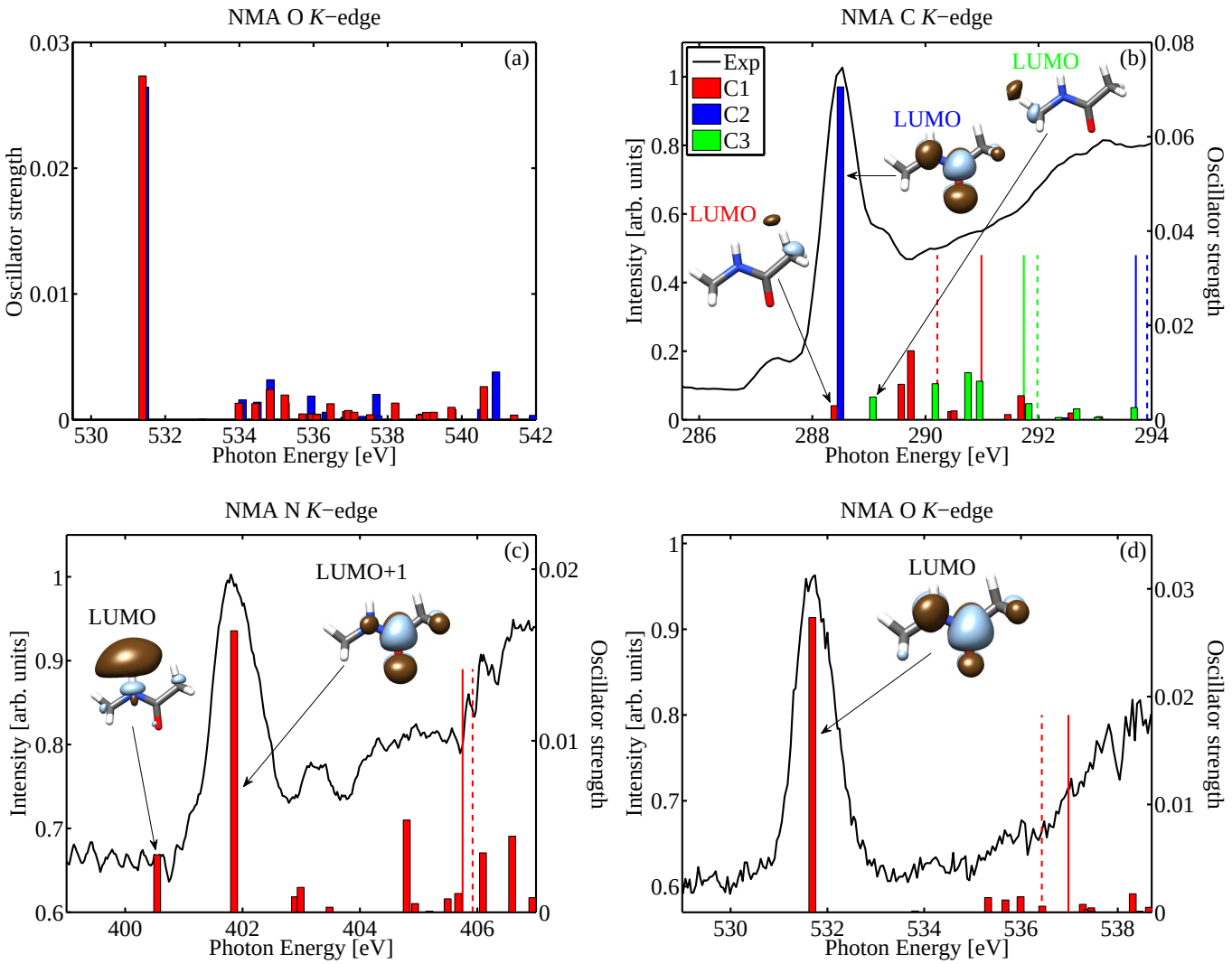

Fig. 2 Theoretically predicted NEXAFS spectra are depicted as bars. (a) NMA O 1*s* spectra calculated for the lowest two *trans*-conformers. The experimental *K*-shell NEXAFS spectra reported in ref.[8] are shown by the solid lines in (b) and (c) panels for C and N *K*-edges, respectively. Panel (d) presents the O 1*s* NMA STEX spectrum (solid curve) remeasured during the current study (see text for more details). The vertical dashed and solid lines present the ΔHF theoretically predicted and experimentally measured core IP values, respectively (Table 1). Note that the theoretical spectra in (b-d) panels were shifted by +0.5 eV, -1.35 eV, and +0.3 eV, respectively. In (b) the numbering of carbon atoms is the same as in Fig. 1(a). The inserts show excited molecular orbitals. In (b-d) left and right side ordinates refer to the experimental and theoretical data, respectively.

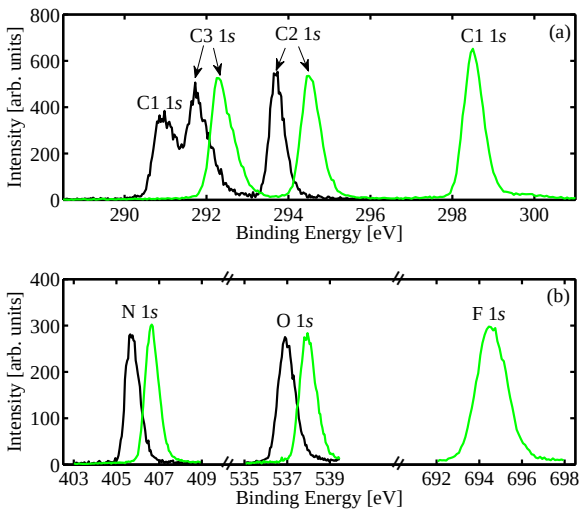

Fig. 3 The experimental XPS spectra for NMA and FNMA are shown by black and green curves, respectively.

values and NEXAFS spectra presented in Tab. 1, Fig. 2 and Fig. 4 for NMA and FNMA, have been calculated only for the lowest energy *trans*-type conformer.

4.2 NMA and FNMA 1s electron IPs

The NMA and FNMA XPS spectra are presented in Fig. 3. They show a general positive chemical shift of the C, N and O peaks in the halogenated species, as could be expected because of the high electronegativity of F. The peak intensity of the NMA C1 1*s* peak is smaller, while the band linewidth is larger, compared with the NMA C2 1*s* and C3 1*s* peaks. Since the ionization cross section of the C 1*s* electron should not strongly depend on the molecular chemical environment, this suggests that upon ionization of the NMA C1 1*s* electron a vibrationally excited molecular core-hole state is formed. The experimental IP values derived from the XPS spectra (Fig. 3) are listed in Tab. 1 where they are compared with the theoretical predictions. It can be observed that the ΔMCSCF calculations, including both electron relaxation and electron correlation effects, show, for the full set of *K*-edges, deviations from the experimental values by an average of ≈0.3 eV in NMA, and ≈0.6 eV in FNMA. This is a reasonably good result taking into account that finer contributions originating from relativistic and vibrational effects have been neglected in the calculations.

4.3 FNMA and NMA NEXAFS feature assignment

The experimental FNMA NEXAFS spectra at the C 1*s*, N 1*s*, O 1*s* and F 1*s* edges are shown as black solid curves in Fig. 4 (a-d), respectively. The *K*-shell NMA NEXAFS spectra for the C, N, and O *K*-edges are presented in Fig. 2 (b-d), respectively. The experimental data presented in Fig. 2(b,c) are adopted from Ref.[8] but were re-calibrated based on Refs.[39,40].

4.3.1 C *K*-edge NEXAFS

The experimental C 1*s* edge NEXAFS spectrum of NMA shows a strong peak at 288.5 eV and two shoulders at 287.4 eV and 289.2 eV (see Fig. 2(b)). The theoretical C 1*s* NEXAFS spectrum for NMA shows the strongest peak at 290.7 eV followed by other significantly weaker features at higher energies. An simple comparison of our experimental and STEX results could be performed by shifting the computed spectrum by about -2.2 eV in order to align the main feature in both spectra. The use of a common energy shift for the three (C1,C2,C3) excitation channels, however, would not be fully justified because, as seen in the last column of Tab. 1, the error due to neglecting the screening effect of the excited electron can be strongly site specific for excitations at the C atoms. These values have been obtained for the lowest excited state of each channel; for the additional excited states we can, in first approximation, adopt linearly scaled values converging to zero at the ionization threshold where the screening effect of a very diffuse Rydberg-like orbital is completely negligible. We have then first applied such a separate energy correction to the bound excitation energies of each computed channel spectrum, which is easily handled in the STEX approach, because it is based on an independent channel approximation and gives the full C *K*-edge spectrum as the addition of the three (C1,C2,C3) spectra. Finally the strongest theoretical peak has been aligned to the most intense experimental peak at 288.5 eV by a small common energy shift of +0.5 eV. By comparison with the computed electronic structure of the core excited state the strong peak can be assigned to the C2 1*s* electron excitation to LUMO which has the $\pi^*_{O-C2}\pi^*_{N-C2}$ character. It is also possible to assign the shoulders at 287.4 eV and 289.2 eV of the main peak observed in the experimental data to excitations of C1 $1s\rightarrow\sigma^*_{H-C1}$ and C3 $1s\rightarrow\sigma^*_{H-C3}$, respectively. Our calculations lead to a more accurate assignment in comparison to Ref.[25] where the spectral profile is similar, but no interpretation in terms of site localization of the spectral main features is provided. This is probably related to the apparently missing theoretical prediction of the core ionization thresholds in Ref.[25].

The experimentally measured FNMA C 1*s* NEXAFS spectrum (see Fig. 4(a)) is more structured compared to the spectrum of NMA (see Fig. 2(b)), as the three carbon atoms in FNMA are located in quite different chemical environments. In fact, due to the large electronegativity of the substituent F atoms, all the three C 1*s* binding energies are predicted to move to higher values in comparison with NMA, see Tab. 1. This effect is particularly strong for the C1 atom (the difference in the C1 1*s* IP values for FNMA and NMA is ≈8 eV) and it can be easily predicted to be present also in the NEXAFS spectrum. It should be noted, however, that in FNMA the decrease of the electron density close to the C1 atom due to the presence of the F atoms affects also the STEX potential making it more attractive. As a result, the term values of the C 1*s* excited states are sensibly larger than those in NMA, as can be verified by comparing the C1 spectra in Fig. 2(a) and Fig. 4(a). In order to compare the results of the STEX calculations to the experimental peaks, the theoretical data have been shifted by the same procedure discussed above for the NMA spectra, namely by an energy correcting for the missing screening of each separate channel spectrum and then applying a common energy shift of -0.08 eV to the full spectrum in order to match the most intense band in the experimental and theoretical pro-

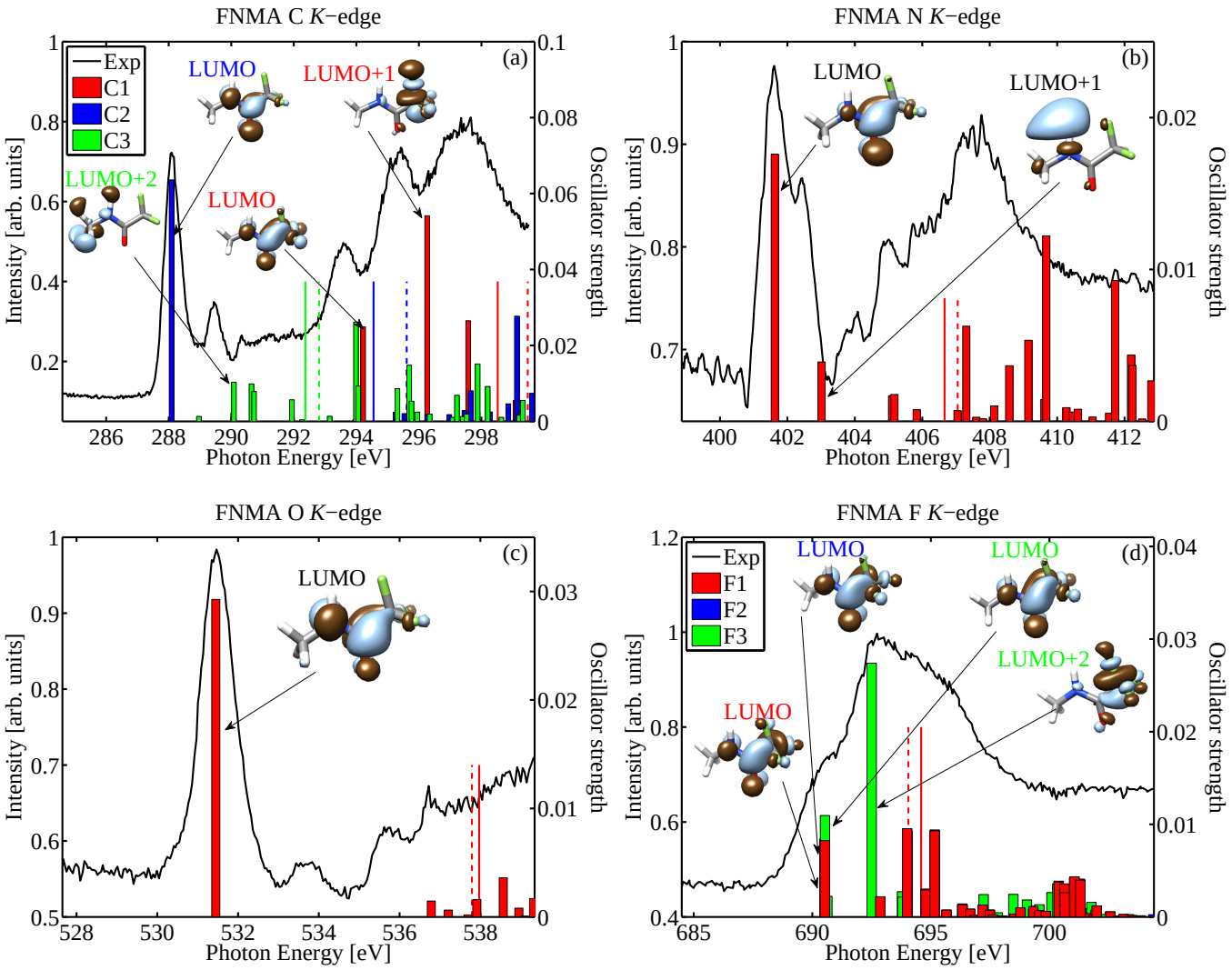

Fig. 4 FNMA C 1*s* (a), N 1*s* (b), O 1*s* (c) and F 1*s* (d) NEXAFS spectra. The experimental data (solid lines) and the theoretical results (bars) are shown together with the measured (solid vertical lines) and ΔHF calculated (vertical dashed lines) IP values. The theoretical spectra in (a-d) are shifted by -0.08 eV, -0.05 eV, +0.4 eV, and 2.5 eV, respectively. In (a) and (d) numbering of carbon and fluorine atoms is the same as in Fig. 1(a) and Fig. 1(d), respectively. The inserts show excited molecular orbitals. Left and right side ordinates refer to the experimental and theoretical data, respectively.

files. Our theoretical predictions suggest that the strong peak in the experimental spectrum located at 288.1 eV is associated with the excitation of the C2 1*s* electron to the LUMO which has the $\pi_{C1-C2}\pi^*_{O-C2}\pi^*_{N-C2}$ character. The other two strongest features at 293.6 eV and 295.4 eV in the experimental spectral profile, peaks that are missing in the corresponding NMA spectrum, are, according to our calculations, assigned to C1 1*s* electron excitation to LUMO ($\pi_{C1-C2}\pi^*_{O-C2}\pi^*_{N-C2}\sigma^*_{C1-F}$) and LUMO+1 ($\sigma^*_{C1-F}$), respectively. Both excitations occur above the C3 1*s* ionization threshold and, in addition to that, the LUMO+1 feature lies also above the C2 1*s* ionization threshold. Finally we assign the less intense peak in the experimental spectrum located at 289.5 eV to excitation of the C3 1*s* electron to LUMO+2 ($\sigma^*_{C3-H}\sigma^*_{O-C2}$). This assignment agrees with the known spectrum of CH_3NH_2 [1] which can be considered as a "building block" for the NMA and FNMA molecules. Also, for the C3 channel (green bars in Fig. 2 and Fig. 4) our calculations predict three almost degenerate excitations of comparable intensity around 289.5 eV which is due to the symmetry splitting by the asymmetric molecular field.

4.3.2 N *K*-edge NEXAFS

The experimental N 1*s* NEXAFS spectra of NMA (Fig. 2(c)) and FNMA (Fig. 4(b)) contain one strong peak, which in the case of FNMA consists of two closely lying peaks. To match the theoretical NEXAFS spectra to the experimental data, the theoretical NMA and FNMA spectra were shifted by -1.35 eV and -0.05 eV, respectively. The theoretical predictions suggest that the strong peak in the experimental spectrum is associated with excitations to LUMO and LUMO+1 and that these orbitals are inverted for the two molecules, *i.e.*, NMA LUMO and FNMA LUMO+1 excited by the N 1*s* electron have σ^*_{N-H} character while NMA LUMO+1 and FNMA LUMO have $\pi^*_{N-C2}\pi^*_{O-C2}$ character. Since the orbital with $\pi^*_{N-C2}\pi^*_{O-C2}$ character has a stronger overlap with the N 1*s* electron orbital, for NMA the oscillator strength of the N 1*s*→LUMO+1 transition is more intense than to LUMO and for FNMA it is opposite. Other weak peaks observed in both experimental spectra below the ionization threshold are assigned to excitations to higher order UMOs of Rydberg character. A previous application [50] of the STEX approach to the NEXAFS N 1*s* spectrum of NMA led to results very similar to the present ones, except for a different intensity distribution among the two lowest excited states. Because the main peak in the NMA experimental spectrum is relatively broad, it cannot be compared directly with these two theoretical findings. Nonetheless, it can be observed that the experimental N *K*-edge NEXAFS spectrum of the glycine amino acid, which is close in structure to NMA, measured with high resolution [47] consists of two resolved peaks separated by about 1.2 eV with the lowest energy peak being remarkably lower in intensity than the the second peak, in agreement with the present findings.

4.3.3 O *K*-edge NEXAFS

The experimental FNMA O 1*s* NEXAFS spectrum (Fig. 4(c)) consists of only one strong peak, while the corresponding NMA spectrum reported by us earlier contained several intense features (see Fig. 3(c) for Ref. [8]). Such a difference is a bit surprising since each molecule contains one oxygen atom located in very similar chemical environments (Fig. 1(a,d)). Indeed, the theoretical calculations predict similar O 1*s* NEXAFS spectra for the two molecules containing only one strong peak. Furthermore, the recent NMA O 1*s* NEXAFS measurements by Lin *et al.* [25] and the STEX calculations of Mukamel *et al.* [50] showed one intense peak. We have therefore re-measured the NEXAFS spectrum of NMA and the results are shown in Fig. 2(d), in which additional intense features are absent. A careful examination of the previously published data led us to the conclusion that the sample and/or gas inlet used then contained a significant amount of water which shows strong resonances at the oxygen *K*-edge [51].

The theoretical NEXAFS spectrum for NMA and FNMA presented with the bars in Fig. 2(d) and Fig. 4(c), respectively, were shifted by +0.3 eV and +0.4 eV, respectively, to match the highest intensity peak in the experimental data. The theory predicts that this peak is associated with excitation of the LUMO which has $\pi^*_{O-C2}\pi^*_{N-C2}$ and $\pi^*_{O-C2}\pi^*_{N-C2}\pi_{C2-C1}$ character for NMA and FNMA, respectively.

4.3.4 F *K*-edge NEXAFS

The F 1*s* experimental NEXAFS spectrum contains one broad feature with a lower energy shoulder but it is mostly structureless (Fig. 4(d)). This can be explained by a multitude of overlapping peaks as well as by the comparatively short lifetime of the F $1s^{-1}$ hole and, possibly, a more complex vibrational envelope. The theoretical spectrum is presented in the same figure as bars and contributions from different F atoms are denoted by different colors. Since the F1 and F2 atoms are symmetric with respect to the molecular plane (see Fig. 1), the corresponding core orbitals are almost degenerate and delocalized on the two atoms; for a more accurate estimation of the core BE at the ΔHF level we performed a localization procedure [52]. The theoretical NEXAFS spectra associated with these two atoms are very similar and hardly distinguishable in the figure.

The lowest energy NEXAFS feature is theoretically assigned to excitations to LUMO from F1, F2 and F3. To match these three features to the lower energy shoulder in the experimental spectrum, the theoretical data were shifted by +2.5 eV. The most intense band at about 690 eV is associated with F3 1*s* excitation to LUMO+2 which has a σ^*_{C1-F3} character and coincides with the highest intensity of the experimental spectrum. The reduced localization of LUMO+1 on F3 leads to a quite weak contribution to the spectrum.

4.4 FNMA ion yield upon core-excitations

In what follows, we will discuss ion yields with the aim of identifying possible correlation between ion abundances and the type of the pre-edge resonances. For such purposes, we consider ionic fragments that originate from singly-charged parent ions formed upon single resonant Auger decays which usually dominate over multiply-charged parent ions. Such a choice is motivated by the fact that fragmentation of singly-charged parent ions is expected to be more site-specific [8,53] and mass spectra contain narrower peaks, because of the smaller amount of the kinetic energy released, making data interpretation less ambiguous. The ion mass

Table 2 Relative abundances (%) of single ionic fragments formed upon core-excitations of FNMA. The data are presented for the most abundant ions.

	C 1*s*				N 1*s*		O 1*s*	F 1*s*
fragment (m/z)	288.1 eV	289.5 eV	293.6 eV	295.4 eV	401.6 eV	402.4 eV	531.5 eV	692.7 eV
CH_2^+ (14)	2.1	3.8	3.0	4.1	14.9	2.5	1.7	3.3
CH_3^+ (15)	12.3	5.5	13.8	19.4	14.9	7.5	21.3	6.5
F^+ (19)	<1.0	<1.0	1.7	1.6	<1.0	<1.0	<1.0	6.2
NHC^+ (27)	6.8	11.8	9.3	10.1	10.1	8.2	4.7	7.9
$NHCH^+$ (28)	31.5	27.5	33.8	38.6	55.7	28.3	39.0	18.2
$NHCH_2^+$ (29)	5.4	4.9	4.6	5.5	6.7	3.9	7.6	3.5
CF^+ (31)	6.5	7.6	13.4	13.5	9.2	7.7	5.0	12.3
CF_2^+ (50)	7.7	10.1	6.4	2.5	9.5	7.1	5.6	5.5
$CHNHCO^+$ (56)	1.3	0.6	1.1	1.8	1.5	5.9	1.7	0.5
CH_3NHCO^+ (58)	11.3	2.4	8.8	13.0	5.0	4.7	6.2	0.7
CF_3^+ (69)	19.9	20.5	5.3	3.6	29.2	36.7	27.1	0.4
$NHCCF_3^+$ (96)	<1.0	<1.0	<1.0	<1.0	<1.0	2.6	1.9	<1.0

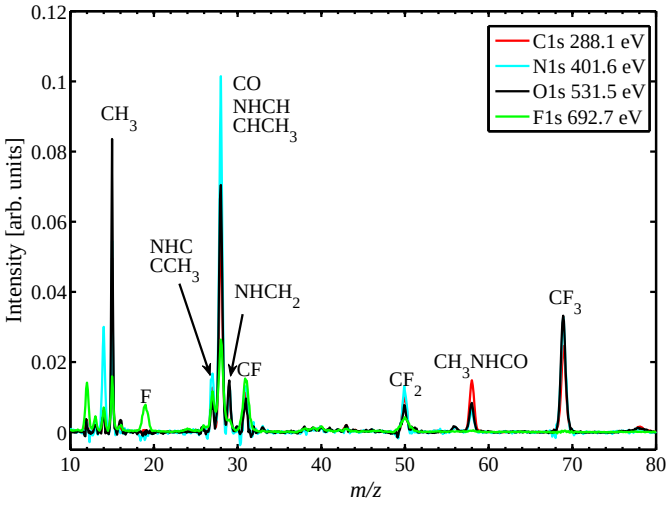

Fig. 5 FNMA total ion mass spectra associated with the strongest excitation resonances at the C, N, O and F K-edges. The data were corrected for the non-resonant contributions. Each spectrum has been normalized to its integrated intensity.

spectra are presented in Fig. 5 for the strongest FNMA NEXAFS peaks at the C, N, O and F K-edges. Ion yields associated with these peaks as well as with several other lower intensity peaks are listed in Tab. 2. As can be seen from Fig. 5 and Tab. 2, intensities of the ion fragments vary depending on which core-shell electron resonance is excited. This indicates that Auger decay following the core-excitation leaves the molecule in different excited states and the molecular fragmentation following the Auger decay is specific with respect to the core excitation. The mass spectra are dominated by the three distinct, relatively strong peaks at $m/z =$ 15, 28, and 69. The peak at $m/z = 15$ is associated with the production of the methyl ion, CH_3^+. By comparing the yield of this ion for the four C K-shell pre-edge resonances listed in Tab. 2, it is seen that the lowest yield is obtained at $h\nu = 289.5$ eV. This can be explained by the FNMA NEXAFS peak assignment which suggests that the 289.5 eV peak is associated with excitation of the C3 1s electron to the LUMO+2 which has an anti-bonding character along the C-H bonds in the methyl moiety *i.e.*, repulsion forces along the C-H bonds diminishes the probability to form CH_3^+.

The peak at $m/z = 28$ can be assigned to the $NHCH^+$ fragment. Although this peak can also originate from the CO^+ and $C_2H_4^+$ fragments, based on the previous peak assignment performed for NMA[25], these fragments are less important. The $NHCH^+$ fragment can be produced in two ways, either by cleavage of the peptide bond, C(=O)-NH, accompanied by ejection of two hydrogen atoms or by detaching an O atom, CF_3 moiety, CH_2 followed by rearrangement. We assume the formation of the $NHCH^+$ through the cleavage of the peptide bond to be most likely. Note that the increased abundances at $m/z = 14$ and 28 for the 401.6 eV excitation energy is due to residual N_2 in the chamber.

From Tab. 2, it follows that the yield of the $NHCH^+$ fragment is significantly enhanced when the N 1s electron is excited to the LUMO (401.6 eV) which has an anti-bonding character along the peptide bond. Such an observation is an evidence for site-specific fragmentation, *i.e.*, the excitation of a core electron to an anti-bonding orbital localized on the site of the core orbital leads at the same time to a strong absorption intensity and a strong propensity to break the local molecular bond.

The CF_3^+ fragment has m/z of 69 and it is one of the most abundant fragments in the ion mass spectra. The yield of this ion tends to decrease significantly at 293.6 eV and 295.4 eV for the C K-edge as well as when F 1s electrons are excited. Such a tendency can be explained by the fact that at these excitation energies the core electrons are promoted to the UMOs that have anti-bonding characters along the C-F bonds and, thus, the chance to produce CF_3^+ is lower. The yield of the F^+ fragment is opposite to that of CF_3^+ which can be explained in a similar way that production of F^+ enhances when the C-F anti-bonding UMOs are excited. The enhanced production of F^+ is another evidence for the site-specific fragmentation, as, for example, 293.6 eV and 295.4 eV excitations are associated with the carbon atom from the CF_3 moiety. We note that there are also contributions to the 293.6 eV peak originating from the C3 1s excitations (Fig. 4a). However, since such excitations are of Rydberg characters, the site-specific fragmentation is most likely associated with the non-Rydberg orbital, *i.e.*, C1 $1s \rightarrow$ LUMO.

It is interesting to note that a rather weak peak located at $m/z =$ 96 appears when the O 1s electron is excited. Most likely this peak is associated with the $NHCCF_3^+$ fragment. If it is indeed so, formation of this fragment at the O 1s edge provides additional evidence for a site specific fragmentation, *i.e.*, by exciting the O

1*s* electron to the LUMO which has an anti-bonding character along the C-O bond, this bond is ruptured accompanied by the detachment of the methyl moiety.

5 Conclusions

NMA and FNMA, as peptide model systems, were studied experimentally by means of XPS and NEXAFS spectroscopies at the C, N, O and F *K*-edges, in direct comparison with *ab initio* numerical calculations. The vertical core IPs were calculated by the ΔHF method that includes the main effect of electronic relaxation and by the ΔMCSCF method that adds the effect of electron correlation. The values predicted by the ΔMCSCF calculations have proven to be in excellent agreement with the experimental measurements, with deviations of a few tenths of eV for most of the edges. The simulations of the photoabsorption spectra, based on the STEX approach, lead to an accurate assignment of the main features of the experimental profiles and to their association to the electronic structure of the virtual orbitals occupied by the excitation process. This allowed us to identify their anti-bonding character along the different molecular bonds and foresee a possible selective dissociation of the peptide bond through a specific tuning of the photon energy. The main limitation of the STEX approximation, namely the disregard of the electronic screening operated by the excited electron on the target ion electronic density was investigated in detail by ΔMCSCF calculations for the lowest excited state of each excitation channel. It was shown quantitatively that this screening effect can be very different for chemically shifted atoms; this finding puts into question the generally used common energy correction of the theoretical spectra for their comparison with experimental data.

We have also investigated the fragmentation patterns of FNMA upon resonant excitation of several different *K*-shell pre-edge resonances, where we have observed in some cases a correlation with the UMO electron density distributions, implying that the molecular bonds with anti-bonding characters were preferentially ruptured. Such an observation points towards resonant spectator type Auger decay. However, with the current experimental set-up we were not able to distinguish between spectator and participator Auger electrons. In the future we plan to perform resonant Auger electron-ion coincidence measurements on FNMA to unambiguously identify molecular fragmentation patterns associated with spectator Auger decay channels.

Acknowledgements

This work has been financially supported by the Swedish Research Council (VR) and the Knut and Alice Wallenberg Foundation, Sweden. P.S. acknowledges financial support from the the Stockholm-Uppsala centre for free electron laser research. L.S. thanks the CNR-IOM Institute for the financial support under the EUROFEL Design Study Project. The research leading to these results has received funding from the European Community's Seventh Framework Programme (FP7/2007-2013) under grant agreement 312284 (CALIPSO). The authors also acknowledge the open access contribution of the Research Infrastructure (RI) Elettra.

References

1 J. Stöhr, *NEXAFS Spectroscopy*, Springer Series in Surface Sciences 25, Ed.s G. Erti, R. Gomer, D. L. Mills, Springer-Verlag, Berlin, Heildeberg, New York, (1992).
2 W. D. Price, P. D. Schnier, and E. R. Williams, Anal. Chem. **68**, 859 (1996).
3 J. A. Zimmerman, C. H. Watson, and J. R. Eyler, Anal. Chem. **63**, 361 (1991).
4 W. D. Bowers, S. S. Delbert, R. L. Hunter, and R. T. McIver Jr., J. Am. Chem. Soc. **106**, 7288 (1984).
5 M. S. Thompson, W. Cui, and J. P. Reilly, Angew. Chem. Int. Ed. **43**, 4791 (2004).
6 D. F. Hunt, W. M. Bone, J. Shabanowitz, J. Rhodes and J. M. Ballard, Anal. Chem. **53**, 1704 (1981).
7 E. R. Williams, K. D. Henry, F. W. McLafferty, J. Shabanowitz, and D.F. Hunt, J. Am. Soc. Mass Spectrom. **1**, 413 (1990).
8 P. Salén *et al.*, Phys. Chem. Chem. Phys. **16**, 15231 (2014).
9 X. J. Liu, G. Prümper, E. Kukk, R. Sankari, M. Hoshino, C. Makochekanwa, M. Kitajima, H. Tanaka, H. Yoshida, Y. Tamenori, and K. Ueda, Phys. Rev. A **72**, 042704 (2005).
10 A. Naves de Brito, R. Feifel, A. Mocellin, A.B. Machado, S. Sundin, I. Hjelte, S. L. Sorensen, and O. Björneholm, Chem. Phys. Lett. **309**, 377 (1999).
11 A. Naves de Brito, S. Sundin, R. R. Marinho, I. Hjelte, G. Fraguas, T. Gejo, N. Kosugi, S. Sorensen, and O. Björneholm, Chem. Phys. Lett. **328**, 177 (2000).
12 K. Ueda, M. Simon, C. Miron, N. Leclercq, R. Guillemin, P. Morin, and S. Tanaka, Phys. Rev. Lett. **83**, 3800 (1999).
13 P. Erman, A. Karawajczyk, E. Rachlew, M. Stankiewicz, and K. Y. Franzen, J. Chem. Phys. **107**, 10827 (1997).
14 P. Morin, M. Simon, C. Miron, N. Leclercq, E. Kukk, J.D. Bozek, and N. Berrah, Phys. Rev. A **61**, 050701 (2000).
15 J. H. D. Eland, P. Linusson, M. Mucke and R. Feifel, Chem. Phys. Lett. **548**, 90 (2012).
16 C. Miron, M. Simon, N. Leclercq, D. L. Hansen, and P. Morin, Phys. Rev. Lett. **81**, 4104 (1998).
17 A. Mocellin, K. Wiesner, S.L. Sorensen, C. Miron, K. Le Guen, D. Céolin, M. Simon, P. Morin, A.B. Machado, O. Björneholm, and A. Naves de Brito, Chem. Phys. Lett. **435**, 214-218 (2007).
18 H. Fukuzawa, G. Pruemper, X.-J. Liu, E. Kukk, R. Sankari, M. Hoshino, H. Tanaka, Y. Tamenori, and K. Ueda, Chem. Phys. Lett. **436**, 51 (2007).
19 E. Itälä, D.T. Ha, K. Kooser, M.A. Huels, E. Rachlew, E. Nommiste, U. Joost and E. Kukk, J. Electron Spectrosc. Relat. Phenom. **184**, 119 (2011).
20 C. Nicolas and C. Miron, J. Electron Spectrosc. Relat. Phenom. **185**, 267 (2012).
21 T. Hatamoto, M. Matsumoto, X.J. Liu, K. Ueda, M. Hoshino, K. Nakagawa, T. Tanaka, H. Tanaka, M. Ehara, R. Tamaki, and H. Nakatsuji, J. Electron Spectrosc. Relat. Phenom. **155**, 54 (2007).
22 U. Hergenhahn, J. Phys. B: At. Mol. Opt. Phys. **37**, R89

(2004).
23 X.J. Liu, G. Prumper, F. Gel'mukhanov, N.A. Cherepkov, H. Tanaka, and K. Ueda, J. Electron Spectrosc. Relat. Phenom. **156**, 73 (2007).
24 U. Hergenhahn, O. Kugeler, A. Rudel, E.E. Rennie, and A.M. Bradshaw, J. Phys. Chem. A **105**, 5704 (20014).
25 Y.-S. Lin, C.-C. Tsai, H.-R. Lin, T.-L. Hsieh, J.-L. Chen, W.-P. Hu, C.-K. Ni, and C.-L. Liu, J. Phys. Chem. A **119**, 6195 (2015).
26 M.W.D. Hanson-Heine, M.W. George, and N.A. Besley, J. Chem. Phys. **138**, 064101 (2013).
27 L. Triguero, L.G.M. Pettersson, and H. Ågren, Phys. Rev. B, PRB **58**, 8097 (1998).
28 H. Ågren, V. Carravetta, O. Vahtras, and L.G.M. Pettersson, Theor. Chem. Acc. **97**, 14 (1997).
29 M. Stener, G. Fronzoni, and M. de Simone, Chem. Phys. Lett. **373**, 115 (2003).
30 V. Carravetta and H. Ågren, *Computational x-ray spectroscopy in Computational Strategies for Spectroscopy: From Small Molecules to Nano Systems*, John Wiley & Sons, Inc., Ed. V. Barone, Hoboken, NJ, USA, (2011).
31 U. Ekström, P. Norman, V. Carravetta, and H. Ågren, Phys. Rev. Lett. **97**, 143001 (2006).
32 U. Ekström, P. Norman, and V. Carravetta, Phys. Rev. A **73**, 022501 (2006).
33 H. Ågren, V. Carravetta, O. Vahtras, and L.G.M. Pettersson, Chem. Phys. Lett. **222**, 75 (1994).
34 R. R. Blyth, R. Delaunay, M. Zitnik, J. Krempasky, R. Krempaska, J. Slezak, K. C. Prince, R. Richter, M. Vondracek, R. Camilloni, L. Avaldi, M. Coreno, G. Stefani, C. Furlani, M. de Simone, S. Stranges, M.-Y. Adam, J. Electron Spectrosc. Relat.Phenom.**101-103**, 959 (1999).
35 M. Tronc, G. C. King, and F. H. Read, J. Phys. B **12**, 137 (1979).
36 M. Tronc, G. C. King, and F. H. Read, J. Phys. B **13**, 999 (1980).
37 K. C. Prince, L. Avaldi, M. Coreno, R. Camilloni, and M. de Simone, J. Phys. B **32**, 2551 (1999).
38 U. Arp, K. Iemura, G. Kutluk, T. Nagata, S. Yagi, and A. Yagishita, J. Phys. B **32**, 1295 (1999).
39 T. K. Sham, B. X. Yang, J. Kirz, and J. S. Tse, Phys. Rev. A **40**, 652 (1989).
40 S. Fatehi, C. P. Schwartz,1 R. J. Saykally, and D. Prendergast, J. Chem. Phys. **132**, 094302 (2010).
41 Dalton, a molecular electronic structure program, Release Dalton2013.X (2013), see http://daltonprogram.org.
42 W.J. Hunt, and W.A.III Goddard, Chem. Phys. Lett. **3**, 414 (1969).
43 N. Kosugi, and H. Kuroda, Chem. Phys. Lett. **74**, 490 (1980).
44 N. Kosugi, Theor. Chim. Acta **72**, 149 (1987).
45 N.G. Mirkin, S. Krimm, J. Mol. Struc. **242**, 143 (1991).
46 A.D. Becke, J. Chem. Phys. **98**, 5648 (1993).
47 A. Schaefer, H. Horn, and R. Ahlrichs, J. Chem. Phys. **97** 2571 (1992).
48 M.W. Schmidt, K.K. Baldridge, J.A. Boatz, S.T. Elbert, M.S. Gordon, J.H. Jensen, S. Koseki, N. Matsunaga, K.A. Nguyen, S. Su, T.L. Windus, M. Dupuis, and J.A. Montgomery, J. Comput. Chem. **14**, 1347 (1993).
49 O. Plekan, V. Feyer, R. Richter, M. Coreno, M. de Simone, K.C. Prince, and V. Carravetta, Chem. Phys. Lett. **442**, 429 (2007).
50 D. Healion, H. Wang, and S. Mukamel, J. Chem. Phys. **134**, 124101 (2011).
51 Ph. Parent, C. Laffon, C. Mangeney, F. Bournel, and M. Tronc, J. Chem. Phys. **117**, 10842 (2002).
52 L.S. Cederbaum and W, Domcke, J. Chem. Phys. **66**, 5084 (1977).
53 P. Salén *et al.*, J. Chem. Phys. **143**, 134302 (2015).